Transient Stability Analysis and Virtual Power Compensation of a Virtual Synchronous Generator Under Low-Voltage Fault

Bo Long, *Senior Member, IEEE*, ChengKun Hu, ZhiHao Chen, Jiefeng Hu, *Senior Member, IEEE*, and José Rodríguez, *Life Fellow, IEEE*

***Abstract*—Virtual synchronous generators (VSGs) demonstrate similar damping and inertia characteristics to traditional synchronous generators, thereby enhancing their ability to support grid voltage and frequency. However, VSGs face challenges related to overcurrent and power angle instability during low-voltage fault conditions. To enhance the low-voltage fault ride-through capability of VSGs, this article introduces a virtual power compensation (VPC) strategy combined with an enhanced current limiting method. First, the transient stability of VSGs with current limiting is analyzed to reveal its instability mechanism. Second, the operational mechanism of the proposed VPC strategy in enhancing transient stability is examined. By means of phase portraits, the effect of transient stability improvement by the VPC is described. Additionally, to facilitate the selection of control parameters, a detailed quantitative analysis has been conducted. Finally, hardware-in-the-loop experiments validate the effectiveness of the proposed control scheme.**

***Index Terms*—Low-voltage faults, transient stability, virtual power compensation (VPC), virtual synchronous generator (VSGs).**

NOMENCLATURE

VSG	Virtual synchronous generator.
VPC	Virtual power compensation.
HIL	Hardware-in-the-loop.
GFM	Grid-forming.
VPA	Virtual power angle.
PCC	Point of common coupling.

Manuscript received 12 February 2024; revised 8 April 2024 and 23 May 2024; accepted 1 July 2024. Date of publication 4 July 2024; date of current version 4 September 2024. This work was supported in part by the Natural Science Foundation of Sichuan Province under Grant 23NSFSC0294, Guangdong Provincial Key Laboratory of New Technology for Smart Grid, China Southern Power Grid Technology Co., Ltd. Guangzhou, Guangdong 510080, China, in part by Guangdong Basic and Applied Basic Research Foundation under Grant 2023A1515240058, and in part by Funding for Chengdu Science and Technology Bureau Level International Cooperation Projects under Grant 2023-GH02-00014-HZ. Recommended for publication by Associate Editor A. Kuperman. *(Corresponding author: Bo Long.)*

Bo Long, ChengKun Hu, and ZhiHao Chen are with the School of Mechanical and Electrical Engineering, University of Electronic Science and Technology of China, Huzhou 611731, China, also with the Yangtze Delta Region Institute (Huzhou), University of Electronic Science and Technology of China, Huzhou 313001, China, also with the Institute of Electronic and Information Engineering, University of Electronic Science and Technology of China, Guangdong 523808, China, and also with the The MOE Key Laboratory of Special Machine and High Voltage Apparatus, Shenyang University of Technology, Shenyang 110870, China (e-mail: longbouestc1980@126.com; 202221040320@std.uestc.edu.cn; 202221040319@std.uestc.edu.cn).

Jiefeng Hu is with the Faculty of Centre for New Energy Transition Research, Federation University Australia, Mount Helen, VIC 3350, Australia (e-mail: j.hu@federation.edu.au).

José Rodríguez is with the Faculty of Engineering, Universidad Andres Bello, Santiago 8370146, Chile (e-mail: jose.rodriguez@unab.cl).

Color versions of one or more figures in this article are available at https://doi.org/10.1109/TPEL.2024.3423445.

Digital Object Identifier 10.1109/TPEL.2024.3423445

I. INTRODUCTION

RENEWABLE energy offers the advantages of being clean, low-carbon, and environmentally friendly. This has led to the large-scale integration of renewable energy power generation units into the power grid, gradually shaping a modern power system characterized by synchronous generators and power electronic devices [1], [2], [3]. Grid-following converters, serving as the primary power interface units, play a crucial role in converting renewable energy-generated power into ac form for injection into the grid. Despite their pivotal role, grid-following converters lack the inherent inertia and damping characteristics of traditional synchronous generators. This limitation results in weaker support for frequency and voltage, posing significant challenges to the stable operation of power systems. Virtual synchronous generators (VSGs) have emerged as a solution to this issue by providing virtual inertia and damping support to the system by emulating the operational characteristics of synchronous generators [4], [5], [6]. As a result, VSGs have garnered significant interest among researchers in recent years.

However, the related technology of VSG is still in its infancy and faces many stability problems. Among these, the large-signal transient stability issues caused by grid voltage sags, transmission line faults, and load fluctuations involve complex nonlinear analysis and continue to present a challenge [7], [8], [9]. Once a fault occurs, the active power reference and the maximum output power of the VSG determine the existence of the operating point. If the active power reference exceeds the maximum output power, a stable operating point may not exist, leading to system destabilization [10]. The overcurrent capability of VSGs is much weaker than that of synchronous generators. Therefore, the controller must establish a current limiting mechanism, which results in a reduction of the maximum output power of the VSG. This, in turn, degrades the transient stability and increases the risk of system destabilization [11], [12], [13].

Considering those issues, some studies examine the impact of current limiting on the transient stability of grid-forming (GFM) converters. For example, in [14], an equivalent circuit model of a GFM converter with a loop current limiter was developed, and its transient stability was analyzed. The results indicated that the GFM converter can be simplified to a voltage source with an equivalent resistor. However, stable operation still requires ensuring that the active power reference does not exceed the maximum output power. In [15], the effects of different current limiting strategies on the transient stability of VSGs were investigated. The results indicate that the current limiting of VSGs significantly affects their power output during and after faults. The current limiting strategy for q-axis current priority provides a larger transient stability margin compared to the current vector angle method and the d-axis current priority method. However, no corresponding transient stability enhancement strategy is proposed, nor are the effects of different current limiting methods on fault recovery addressed. In [16], a transient stability analysis of VSGs equipped with a q-axis priority current limiter has been performed. The analysis indicates that, apart from the instability caused by the positive feedback of the primary controller, the VSG may also face instability following a large disturbance due to the failure of the internal voltage controller. However, again, no strategy is proposed to enhance the transient stability under large disturbances.

When VSGs are unable to stabilize under large disturbances, they are disconnected from the grid to prevent further deterioration. However, with the increasing penetration of power electronics in modern grids, VSGs are needed to provide voltage and frequency support to the grid [17]. Therefore, VSGs should have a certain low-voltage fault ride-through capability. Generally, there are three main approaches to enhancing the stability of grid-connected converters under large disturbances, which are as follows.

1) Switching the control structure to grid-following mode during faults. The scheme of switching to grid-following control during faults was proposed in [18], [19], and [20]. During faults, overcurrent suppression of the output current can be achieved by directly limiting the output current. However, this requires complex parameter selection and online fault detection algorithms. Moreover, the switching between the two operating modes will incur oscillations that cannot be recovered after fault removal.
2) Limiting the converter current by using a virtual impedance. This technique utilizes the virtual impedance for the internal current and voltage references to limit the current [21], [22], [23]. The current limitation heavily depends on the fault location and the selected virtual impedance, which is highly influenced by the degree of voltage sag, so it is difficult to precisely limit the current to the desired value. This limitation significantly hinders its practical application.
3) Adjusting the power reference during faults. In [13] and [24], enhancing the transient stability of the GFM converter can be achieved by lowering the power reference during faults. However, this approach results in a decrease in active power transfer. It is unfavorable for frequency regulation and also may lead to system breakdown [7]. The objective is to effectively, reliably, and optimally utilize converter currents under any fault [11], [12].

To address the existing challenges in the transient stability enhancement strategy for VSGs, such as the complexity of switching to grid-following mode, the difficulty in accurately limiting current with virtual impedance, and the decrease in active power transfer when adjusting power references. This article analyzes the transient stability of the VSG with current limiting to uncover its destabilization mechanism. The focus is on the dynamic characteristics of the virtual power angle (VPA) during faults, which depict the synchronization properties of VSG with the grid. Furthermore, a virtual power compensation (VPC) strategy is introduced to enhance power angle stability during low-voltage faults. When coupled with the improved current-limiting control strategy, it enables postfault recovery, thereby significantly enhancing the low-voltage fault ride-through capability of the VSG. The proposed strategy is straightforward to implement, as it does not require fault detection or online power reference adjustment, and it optimizes the output capacity of the VSG during fault conditions. The main contributions of this article are summarized as follows.

1) Starting from the dynamic response of VSGs encountering a large disturbance (e.g., voltage sag), the transient behaviors of the VSG are qualitatively analyzed by using the power angle characteristic curve and phase diagrams theory. This analysis reveals the reason for transient instability in VSGs during voltage sag.
2) The proposed VPC strategy enhances the transient stability of VSG by maintaining synchronization with the grid during voltage sag periods, improving postfault recovery through an improved current limiting method. This approach effectively addresses transient instability in VSGs under large disturbances, enabling fault recovery without the need for fault detection, online control switching, or power reference adjustment.

The rest of this article is organized as follows. Section II outlines the configuration of the VSG and its equivalent model. Section III qualitatively examines the transient stability of the VSG following grid voltage sag in two scenarios, validating the findings through simulations. In Section IV, a qualitative analysis of the operational principles of the VPC strategy is conducted, and the influence of VPC parameters is explored. To validate the effectiveness of the proposed method, hardware-in-the-loop (HIL) comparative experiments are conducted in Section V. Finally, Section VI concludes this article.

II. Modeling of Grid-Connected VSG

A. Configuration of VSG

Fig. 1 shows the power circuit topology of the VSG and its control block diagram. The three-phase voltage source inverter is connected to the three-phase ac grid through an LC filter consisting of the inductor L_1 and the capacitor C_1. L_{line}, R_{line}, I_{1abc}, I_{abc}, E_{abc}, and V_g are the line inductor, line resistor, inverter bridge output current, point of common coupling (PCC) current, PCC voltage, and grid voltage, respectively. V_{dc} is the

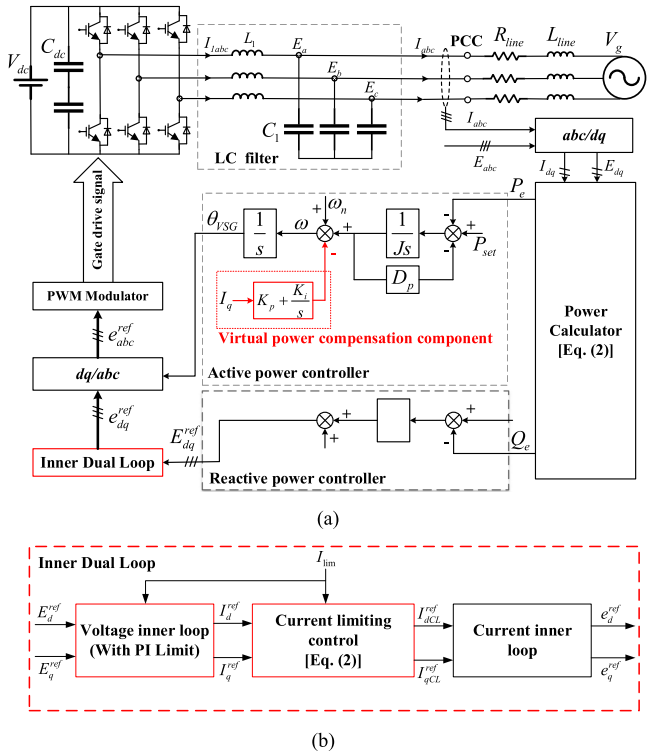

Fig. 1. Configuration of VSG. (a) General framework diagram. (b) Inner dual loop.

dc-link voltage. E_{dq} and I_{dq} are obtained by park transformation for E_{abc} and I_{abc}, respectively, to facilitate the subsequent power calculation and generation of control laws.

The phase and voltage reference amplitudes of the VSG are generated by the active and reactive power controllers, respectively. The traditional mathematical expression of VSG can be written as [25]

$$\begin{cases} \omega - \omega_n = \frac{1}{Js+\mathrm{D}_p}(P_{set} - P_e) \\ E_d^{ref} - V_0 = \frac{1}{K_q s}(\mathrm{Q}_{set} - \mathrm{Q}_e) \\ \delta = \frac{1}{s}(\omega - \omega_n) \end{cases} \tag{1}$$

where P_{set} and Q_{set} are the active and reactive power references, and P_e and Q_e are the instantaneous active and reactive power output of the VSG, respectively, calculated as follows:

$$\begin{cases} P_e = \frac{3}{2}(E_d I_d + E_q I_q) \\ Q_e = \frac{3}{2}(E_q I_d - E_d I_q) \end{cases} \tag{2}$$

where J and D_p are the virtual inertia and damping coefficient of the active power loop, respectively, and K_q is the integral coefficient of the reactive power loop. ω_n and V_0 are the rated frequency and amplitude of the output voltage, respectively. ω and δ are the angular frequency and VPA of the active power controller, respectively, and E_{dq}^{ref} is the reference voltage generated by the reactive power controller.

To prevent overcurrent from damaging the electronics in the VSG, a current limiting link needs to be added to the inner loop [see Fig. 1(b)]. There are two commonly used current

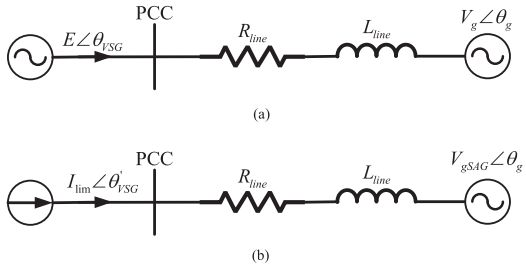

Fig. 2. Equivalent model of a VSG. (a) Normal operation. (b) Current limiting operation under fault.

limiting strategies in VSG control, i.e., current-referenced current limiting and voltage-referenced current limiting with virtual impedance [11], [21]. In this article, a current limiting method that preserves the dynamics of the d- and q-axis currents is adopted, which is specified as

$$A_m = \sqrt{\left(I_d^{ref}\right)^2 + \left(I_q^{\mathrm{ref}}\right)^2}$$

$$(I_{dCL}^{\mathrm{ref}}, I_{qCL}^{\mathrm{ref}}) = \begin{cases} \left(I_d^{\mathrm{ref}} \times \frac{I_{\mathrm{lim}}}{A_m}, I_q^{\mathrm{ref}} \times \frac{I_{\mathrm{lim}}}{A_m}\right) \mathrm{A_m} \geq \mathrm{I_{lim}} \\ (I_d^{\mathrm{ref}}, I_q^{\mathrm{ref}}) \mathrm{A_m} < \mathrm{I_{lim}} \end{cases} \tag{3}$$

In (3), I_d^{ref} and I_q^{ref} are the outputs of the voltage loop, and A_m is the amplitude of the output of the voltage loop. I_{lim} represents the maximum allowable current for output. The final output and integral link of the voltage loop are both constrained, with limiting values of $(-I_{\mathrm{lim}}, +I_{\mathrm{lim}})$. The reference current outputs (I_{dCL}^{ref} and I_{qCL}^{ref}) after limiting are used to generate the final voltage references (e_d^{ref} and e_q^{ref}) by the current loop.

It is worth noting that the current limiting strategy in (3) is different from the traditional priority-based current limiting strategy. It imposes an overall limit on the current based on control requirements, rather than biasing toward the d-axis or q-axis as traditional ways [11], [16], [26]. Thus, it preserves the dynamic characteristics of current regulation to some extent.

B. Equivalent Model of VSG

Analogous to the power angle in traditional synchronous generators, the phase angle difference between the VSG control coordinate system and the grid coordinate system can be defined as δ. If the phase angle of the VSG controller output is denoted as θ_{VSG} and the phase angle of the grid is θ_g, then δ satisfies

$$\delta = \theta_{\mathrm{VSG}} - \theta_{\mathrm{g}}. \tag{4}$$

According to (4), the equivalent simplified model of VSG connected to the infinite grid during normal operation is shown in Fig. 2(a), where $E\angle\theta_{\mathrm{VSG}}$ represents the equivalent output of the VSG. Its vector diagram is shown in Fig. 3(a). It should be noted that in this article, the vector diagram is drawn with the output voltage of VSG, i.e., the voltage at the PCC point, as the reference. Accordingly, the active and reactive power output from the VSG during normal operation can be derived as

$$\begin{cases} P_e = \frac{3}{2}\frac{\mathrm{R}_\Sigma(E^2 - EV_g\cos\delta) + EV_g X_\Sigma \sin\delta}{{\mathrm{R}_\Sigma}^2 + X_\Sigma^2} \\ Q_e = \frac{3}{2}\frac{X_\Sigma(E^2 - EV_g\cos\delta) - EV_g R_\Sigma \sin\delta}{\mathrm{R}_\Sigma^2 + X_\Sigma^2} \end{cases} \tag{5}$$

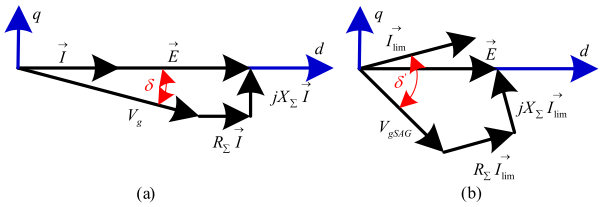

Fig. 3. Vector diagram of VSG. (a) Normal operation. (b) Current limiting operation under fault.

where $R_\Sigma = R_{\text{line}}$ and $X_\Sigma = X_{\text{line}}$.

When a low-voltage fault occurs, the external characteristics are similar to those of a current source if the VSG output current is limited. The equivalent circuit model is shown in Fig. 2(b), where $I_{\text{lim}}\angle\theta'_{\text{VSG}}$ represents the equivalent output of the VSG. The vector diagram of the VSG is illustrated in Fig. 3(b).

$V_{g\text{SAG}}$ denotes the amplitude of the grid voltage sag, θ'_{VSG} denotes the phase angle of the converter output after current limiting, and δ' denotes the VPA at which the current limiting is reached. The expression of δ' is written as follows:

$$\delta' = \theta'_{\text{VSG}} - \theta_g. \tag{6}$$

Further from Fig. 2(b) and considering that the high-voltage power grid satisfies the inductance much larger than the resistance, the line resistance can be approximated as 0. The active power P_{eCL} of the converter output after current limiting can be approximated as

$$P_{eCL} \approx \frac{3}{2} I_{\text{lim}} V_{g\text{SAG}} \cos\delta'. \tag{7}$$

It can be further shown that the maximum value of power output $P_{e\text{MAX}}$ is

$$\mathrm{P}_{e\text{MAX}} = \frac{3}{2} V_{g\text{SAG}} I_{\text{lim}}. \tag{8}$$

P_e and P_{eCL} can be obtained by approximating and simplifying (5) and (7) as

$$\begin{cases} P_e \approx \frac{3}{2}\frac{EV_g \sin\delta}{\mathrm{X}_\Sigma} \\ P_{eCL} \approx \frac{3}{2} I_{\text{lim}} V_{g\text{SAG}} \cos\delta' \end{cases}. \tag{9}$$

Comparing the two equations in (9), it is observed that $P_e - \delta$ curve exhibits an approximately sinusoidal relationship before reaching the current limit. However, after the current limitation, it becomes a cosine relationship. As a result, the power-angle characteristic curve displays different behaviors.

III. Transient Stability Analysis of VSG Considering Current Limiting

Based on (9), in this section, we will qualitatively analyze the transient stability of the VSG after a voltage sag in the grid, focusing on the dynamic behavior of the VPA to evaluate its power angle stability. Considering the significant differences in power–angle characteristics before and after current limiting, they will be analyzed in two cases.

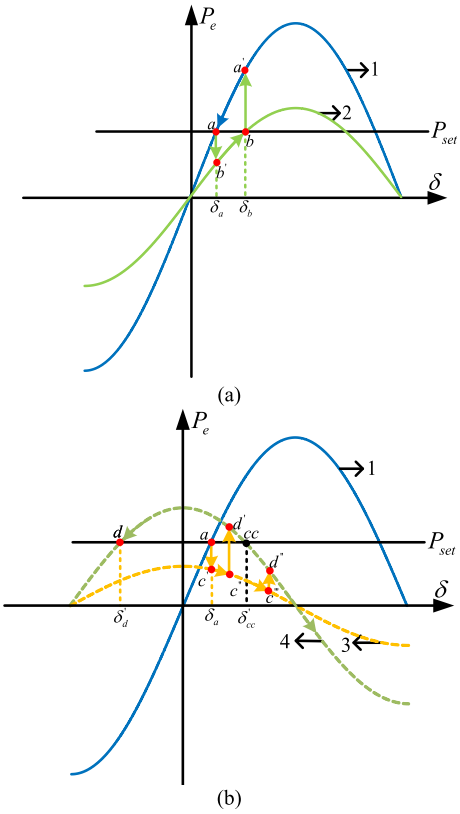

Fig. 4. P_e-δ curve of VSG. (a) $P_{\text{set}} < 1.5 I_{\text{lim}} V_{g\text{SAG}}$. (b) $P_{\text{set}} > 1.5 I_{\text{lim}} V_{g\text{SAG}}$.

A. Voltage Sag With $P_{set} < 1.5 I_{lim} V_{gSAG}$

According to (8), it is known that in this case, the reference power P_{set} is less than the maximal power output of the VSG. The VSG is working in a noncurrent limiting state, and thus at this time, the inverter is working with the normal mode, i.e., the VSG control mode. Fig. 4(a) shows the operating characteristics in this case.

Curve 1 in Fig. 4(a) is the $P_e - \delta$ curve under normal operating conditions and curve 2 in Fig. 4(a) is the $P_e - \delta$ curve after a sag in the grid voltage. Initially, the system works stably at point a. After grid voltage sags, the operating point immediately shifts down to point b' on curve 2 [see Fig. 4(a)]. Since $P_{\text{set}} > P_e$, according to (1), it can be seen that δ will increase to point b along curve 2 [see Fig. 4(a)], ensuring stable operation during this period. If the grid voltage restores to the normal state, the operating point will promptly transition from point b on curve 2 to point a' on curve 1 [see Fig. 4(a)]. Because the output power $P_e > P_{\text{set}}$ at point a', δ will decrease to the operating point, where $P_{\text{set}} = P_e$, specifically point a. Hence, the system is restored to its initial state after disturbance.

Therefore, the change in the operating point of the system during voltage sag with $P_{\text{set}} < 1.5 I_{\text{lim}} V_{g\text{SAG}}$ situation is: $a \to b' \to b \to a' \to a$.

Fig. 5(a) shows the simulation result when the grid voltage level drops from 1.0 to 0.8 p.u., δ of the VSG increases from a to b. When the fault is cleared at any moment, it can go back

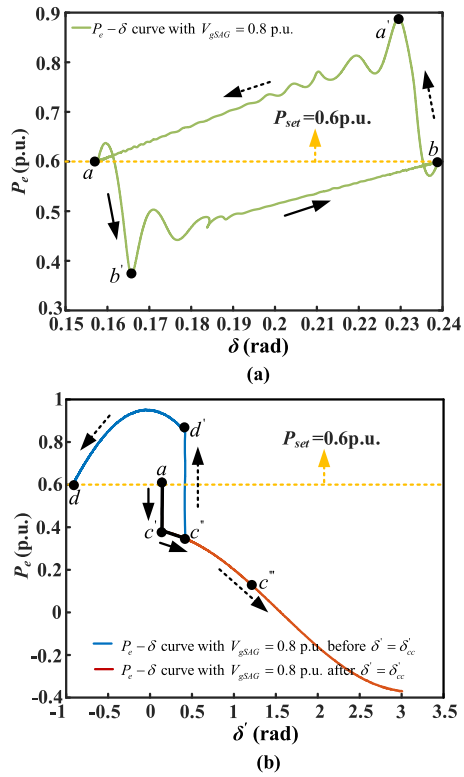

Fig. 5. Simulation results of $P_e-\delta$. (a) $P_{\text{set}} < 1.5I_{\text{lim}}V_{g\text{SAG}}$. (b) $P_{\text{set}} > 1.5I_{\text{lim}}V_{g\text{SAG}}$.

to the initial operation working point a. Therefore, under the condition of satisfying $P_{\text{set}} < 1.5I_{\text{lim}}V_{g\text{SAG}}$, the system not only can autonomously recover after the fault but also operate in the VSG mode, thus having the capability to emulate the operation of synchronous generators.

B. Voltage Sag With $P_{set} > 1.5I_{lim}V_{gSAG}$

According to (8), the maximum power output of VSG is less than the power reference P_{set} during low-voltage faults, leading to the absence of a stable VPA. In other words, the VSG is unable to synchronize with the grid, resulting in system instability.

Curve 3 in Fig. 4(b) shows the $P_e-\delta$ curve of the system current limit operation after the grid voltage sag, and curve 4 in Fig. 4(b) shows the $P_e-\delta$ curve of the system current limit operation after the grid voltage recovery. The system begins stable operation at point a [see Fig. 4(b)]. If a grid voltage sag occurs at this moment, the system will transition from a to c' [see Fig. 4(b)]. Since $P_{\text{set}} > P_e$ at this time, according to (1), it is evident that δ' will increase. At this time, there are the following two situations.

1) The fault is cleared before δ' increases to critical clearing angle δ'_{cc}, which can be calculated by

$$\delta'_{cc} = \arccos\frac{P_{\text{set}}}{1.5I_{\text{lim}}V_g}. \tag{10}$$

For example, when the system is running until c'' and the fault is cleared, the system will quickly run from c'' to d' [see Fig. 4(b)]. Because d' meets $P_{\text{set}} < P_e$, δ' will be reduced until $P_{\text{set}} = P_e$ at point d, indicating that point d is a stable operating point. It is worth noting that, during this period, while the system may remain stable, the converter operates in current limit mode and cannot emulate the operation effect of a synchronous generator.

2) The fault is cleared after $\delta' = \delta'_{cc}$. For example, when the system is running until c''' and the fault is cleared, then $P_{\text{set}} > P_e$ still holds, and δ' will continue to increase to the point where $P_e < 0$ occurs. This situation will result in power oscillations, along with the phenomenon of absorbing power from the grid, exacerbating the degree of grid faults. Therefore, this represents the most severe transient instability.

Therefore, if the fault is cleared before $\delta' = \delta'_{cc}$, then the change in the operating point of the system during voltage sag with $P_{\text{set}} > 1.5I_{\text{lim}}V_{g\text{SAG}}$ situation is: $a \to c' \to c'' \to d' \to d$.

Fig. 5(b) shows the simulation results when the grid voltage drops from 1.0 to 0.5 p.u., satisfying $P_{\text{set}} > 1.5I_{\text{lim}}V_{g\text{SAG}}$. In this case, the VPA will increase, as indicated by the black line. As the system progresses toward c'' and the fault is cleared before $\delta' = \delta'_{cc}$, δ' will begin to decrease until it reaches the new steady-state operating point d. During this phase, the system operates in current limit mode and cannot simulate the operating characteristics of a synchronous generator. If in this case, the fault is cleared at point c''', i.e., after $\delta' = \delta'_{cc}$, δ' will continue to increase, leading to the occurrence of power absorption from the grid. Consequently, at this point, it can be assumed that the system has become completely destabilized.

From the perspective of transient stability, if the maximal active power output $P_{e\text{MAX}}$ exceeds the reference P_{set} in VSG when transient voltage sag occurs, the system will not lose its stability. If $P_{e\text{MAX}} < P_{\text{set}}$, the fault must be cleared in time when no power compensation is processed, otherwise the system will be unstable.

IV. Transient Stability Improvement Through VPA

A. Proposed VPC Strategy

After the previous analysis, it is evident that during large disturbances, the reason for transient instability in VSG is its maximum transmitted power $P_{e\text{MAX}}$ following a low-voltage fault falls below the power reference P_{set}. This discrepancy results in the VSG lacking a stable power angle, thereby causing transient instability due to the desynchronization between the VSG and the grid. For this reason, this article proposes a VPC strategy to enhance transient stability.

The basic idea of VPC is to introduce the q-axis current component, i.e., I_q, and its specific control block diagram is shown in Fig. 6. In normal operation, I_q is approximately 0 and does not influence the power tracking capability of the active loop. However, during fault periods, the I_q feedback loop can act as VPC to prevent VSG from desynchronizing with the grid caused by the maximum output power $P_{e\text{MAX}}$ being less than the power reference P_{set} after a fault. The transient stability analysis of the VSG containing VPC is elaborated as follows.

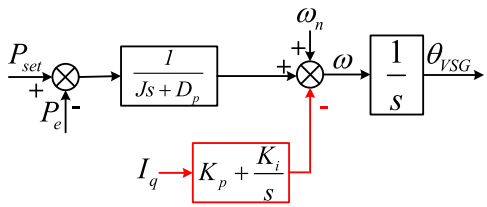

Fig. 6. Block diagram of the proposed VPC.

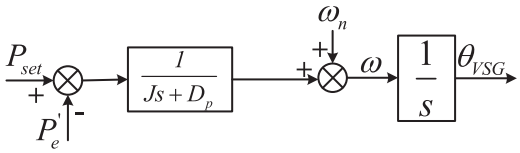

Fig. 7. Block diagram of a simplified VPC.

B. Qualitative Analysis After Introducing VPC

The active loop control equation of the VSG after the introduction of VPC is given in the following equation:

$$s\delta = \omega - \omega_n = \frac{1}{Js+D_p}(P_{\text{set}} - P_e) - I_q\left(K_p + \frac{K_i}{s}\right). \tag{11}$$

After further simplification and equivalence, we obtained Fig. 7 and the following equation:

$$P_e' = P_e + I_q(Js+D_p)\left(K_p + \frac{K_i}{s}\right). \tag{12}$$

The active control equation with the introduction of VPC can be obtained as

$$\dot{\delta} = L^{-1}(s\delta) = L^{-1}\left(\frac{1}{\text{Js}+D_p}(P_{\text{set}} - P_e')\right) \tag{13}$$

where L^{-1} denotes the inverse Laplace transform, and P_e' is the newly defined active output power in the synchronous control containing VPC. From (12), it can be found that the introduction of VPC can achieve VPC. The system can reach a steady state but also needs to satisfy that P_e and I_q are constant and $\dot{\delta}$ and $\ddot{\delta}$ are 0. The expression for $\ddot{\delta}$ is given as follows:

$$\ddot{\delta} = L^{-1}(s^2\delta) = L^{-1}\left(\frac{1}{\text{Js}+D_p}(-sP_e')\right) \tag{14}$$

where sP_e' can be derived as follows:

$$sP_e' = sP_e + s^2 I_q JK_p + sI_q(JK_i + D_pK_p) + I_qD_pK_i. \tag{15}$$

The introduction of VPC enables the power angle to remain stable following a voltage sag, with the converter continuing to primarily transmit active power. This can be approximated as follows:

$$\begin{cases} E_d = V_{g\text{SAG}}\cos\delta + I_dR_\Sigma - I_qX_\Sigma \\ E_q = -V_{g\text{SAG}}\sin\delta + I_qR_\Sigma + I_dX_\Sigma \end{cases}. \tag{16}$$

Since the PCC voltage E is a reference, it can be approximately considered that $E_q = 0$. Additionally, both the line resistance R_Σ and the q-axis current I_q are very small and I_qR_Σ can be neglected, leading to the derivation of an approximate value for I_q as

$$I_{\text{q}} \approx \sqrt{I_{\text{lim}}^2 - \left(\frac{V_{g\text{SAG}}\sin\delta}{X_\Sigma}\right)^2}. \tag{17}$$

The following derivation is to prove that there is a steady-state operating point of VPC after the occurrence of a low-voltage fault. From (14), $\ddot{\delta} = 0$ is equivalent to sP_e', i.e., $\dot{P}_e' = 0$. By applying the inverse Laplace transform to (15), we can obtain $\dot{P}_e'$ as

$$\begin{aligned}\dot{P}_e' = {} & D_pK_iI_q \\ & -\frac{3}{2}I_{\text{lim}}V_{g\text{SAG}}\dot{\delta}\sin\delta - \frac{(JK_i + D_pK_p)}{I_q}\left(\frac{V_{g\text{SAG}}^2\sin\delta\cos\delta}{X_\Sigma^2}\right)\dot{\delta} \\ & -\frac{JK_p}{I_q}\left(\frac{V_{g\text{SAG}}^2\sin\delta\cos\delta}{X_\Sigma^2}\right)\ddot{\delta} + \frac{JK_p}{I_q}\left(\frac{V_{g\text{SAG}}\sin\delta}{X_\Sigma}\right)^2\dot{\delta}^2 \\ & -\frac{JK_p}{I_q}\left(\frac{V_{g\text{SAG}}\cos\delta}{X_\Sigma}\right)^2\dot{\delta}^2 - \frac{JK_p}{I_q^3}\left(\frac{V_{g\text{SAG}}^2\sin\delta\cos\delta}{X_\Sigma^2}\right)^2\dot{\delta}^2 = 0.\end{aligned} \tag{18}$$

From (18), we can get that $I_q = 0$ is the necessary condition to be satisfied when the system reaches the steady state. That is, if no fault occurs that causes the current limiting link to be put into operation, and the system is able to operate stably, then the introduction of VPC will not change the operating point. Since $I_q = 0$ is the steady-state operating point, it does not affect the inertia response and small-signal stability of the VSG during nonfault conditions. It should be noted that the reference value of reactive power Q_{set} needs to be set to 0 to satisfy $I_q = 0$ at this time.

From the previous analysis it is known that when the current limit is reached, the following relationship exists between I_q and δ as

$$\delta = \arcsin\frac{I_qR_\Sigma + \sqrt{I_{\text{lim}}^2 - I_q^2}X_\Sigma}{V_{g\text{SAG}}}. \tag{19}$$

From (19), the relationship curve $I_q - \delta$ can be plotted in Fig. 8. The intersection of this curve with the horizontal axis represents the desired operating point M. If a small disturbance

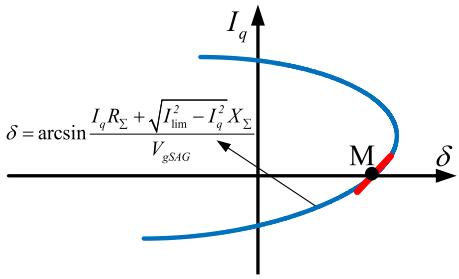

Fig. 8. Qualitative analysis of VPC.

occurs at M, it will cause a small increment in δ. Fig. 8 shows that I_q will also increase. According to (11), it is evident that at this time, $\dot{\delta} < 0$. As a result, the initial increment in δ will diminish, returning to point M. On the contrary, when δ is slightly reduced, I_q will also be reduced. Referring to (11), it can be deduced that $\dot{\delta} > 0$ in this scenario. Consequently, the initially decreased δ will be augmented back to point M. This leads to the conclusion that point M represents the stable equilibrium point of the system.

It is worth noting that the above analysis holds provided that point M cannot be an extreme point of the $I_q - \delta$ curve. The proof is given below.

Taking δ as the dependent variable and I_q as an independent variable, and solving the derivative $\frac{d\delta}{dI_q}$ in (19), we can obtain

$$\frac{d\delta}{dI_q} = \frac{1}{\sqrt{1-k^2}} \frac{\mathrm{R}_\Sigma \sqrt{I_{\lim}^2 - I_q^2} - I_q X_\Sigma}{V_{g\mathrm{SAG}} \sqrt{I_{\lim}^2 - I_q^2}}$$

$$\mathrm{k} = \left(\frac{I_q R_\Sigma + \sqrt{I_{\lim}^2 - I_q^2} X_\Sigma}{V_{g\mathrm{SAG}}} \right). \tag{20}$$

From (20), it can be noted that the existence of $\frac{d\delta}{dI_q}$ is conditional upon $k < 1$. The extremum of k can be determined as follows:

$$k_{\max} = \frac{I_{\lim} \sqrt{X_\Sigma^2 + R_\Sigma^2}}{V_{g\mathrm{SAG}}}. \tag{21}$$

Letting $k_{\max} < 1$, the maximum voltage sag value of $V_{g\mathrm{SAG}}$ can be derived as follows:

$$V_{g\mathrm{SAG}} > I_{\lim} \sqrt{X_\Sigma^2 + R_\Sigma^2}. \tag{22}$$

When $V_{g\mathrm{SAG}} > I_{\lim} \sqrt{X_\Sigma^2 + R_\Sigma^2}$ is satisfied, $\frac{d\delta}{dI_q}$ exists, $\frac{d\delta}{dI_q} > 0$ holds when $I_q = 0$, and let $\frac{d\delta}{dI_q} = 0$, then it leads to the extreme point

$$I_q = \frac{I_{\lim} R_\Sigma}{\sqrt{X_\Sigma^2 + R_\Sigma^2}} > 0. \tag{23}$$

From (23), it can be seen that M is not an extreme point of $I_q - \delta$ curve and the line resistance R_Σ can change the position of the extreme point, thus affecting the transient stability of the system.

Therefore, when $V_{g\mathrm{SAG}} > I_{\lim} \sqrt{X_\Sigma^2 + R_\Sigma^2}$ is satisfied, the proposed VPC can function properly. That is to say, the maximum value of $V_{g\mathrm{SAG}}$ decrease should not be lower than $I_{\lim} \sqrt{X_\Sigma^2 + R_\Sigma^2}$. This implies that the VPC can adapt to extremely low $V_{g\mathrm{SAG}}$ conditions by adjusting $I_{\lim}$. It should also be noted that different VPC parameters such as K_p and K_i need to be selected for different $V_{g\mathrm{SAG}}$ to obtain better transient performance.

In summary, the implementation of VPC improves the transient stability of VSGs. Under low-voltage faults, VPC guarantees the presence of a stable operating power angle in enhancing the system's reliability. Additionally, the introduction of VPC does not adversely affect the operating point during nonfault conditions.

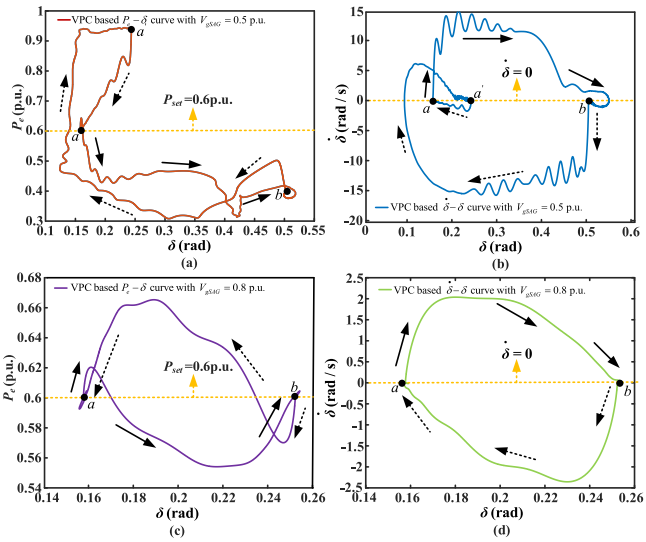

Fig. 9. Simulation results of VSG-based VPC. (a) $P_e - \delta$ curve with $V_{g\mathrm{SAG}} = 0.5$ p.u. (b) $\dot{\delta} - \delta$ curve with $V_{g\mathrm{SAG}} = 0.5$ p.u. (c) $P_e - \delta$ curve with $V_{g\mathrm{SAG}} = 0.8$ p.u. (d) $\dot{\delta} - \delta$ curve with $V_{g\mathrm{SAG}} = 0.8$ p.u.

C. Simulation Verification

Fig. 9 shows the simulation curves after introducing VPC. The simulation adopts the current limiting strategy in (3) and introduces VPC in the active power control loop. The grid voltage level is temporarily reduced from 1.0 to 0.5 p.u. From Fig. 9(a), it can be observed that the VSG works stably at point a before the voltage drops. When the voltage drop occurs, the VSG output power will immediately decrease. Consequently, at this time $P_{\mathrm{set}} > P_e$, the VPA will increase [see Fig. 9(b)]. However, in Fig. 5(b), the critical clearing angle may be exceeded with increasing VPA, leading to complete destabilization or unable to restore the initial state after the fault is cleared. The VSG after the introduction of VPC can operate stably at point b in Fig. 9, which is the equilibrium point M shown in Fig. 8. It can be observed that at point b, the VSG outputs active power $P_e < P_{\mathrm{set}}$, indicating that the introduction of VPC elevates the original actual output P_e to P_e' on the control. This adjustment allows for achieving $P_{\mathrm{set}} = P_e'$, enabling the VSG operate stably even when $P_{\mathrm{set}} > 1.5 I_{\lim} V_{g\mathrm{SAG}}$. This shows the effectiveness of the VPC method.

When the low-voltage fault is cleared, from Fig. 9(a), it is evident that the output active power settles at the maximum active power output point a' after oscillations, and the VPA of the VSG decreases during this period. Due to the limiting strategy in (3), the dynamics of maintaining the d-axis and q-axis currents are retained, thus allowing the voltage–current inner loop to desaturate. Therefore, after desaturation, the VSG will return to the starting point a from a', where $P_{\mathrm{set}} = P_e$ and $\dot{\delta} = 0$ are satisfied. Thus, the improved limiting strategy allows VSG to return to its original state after fault removal.

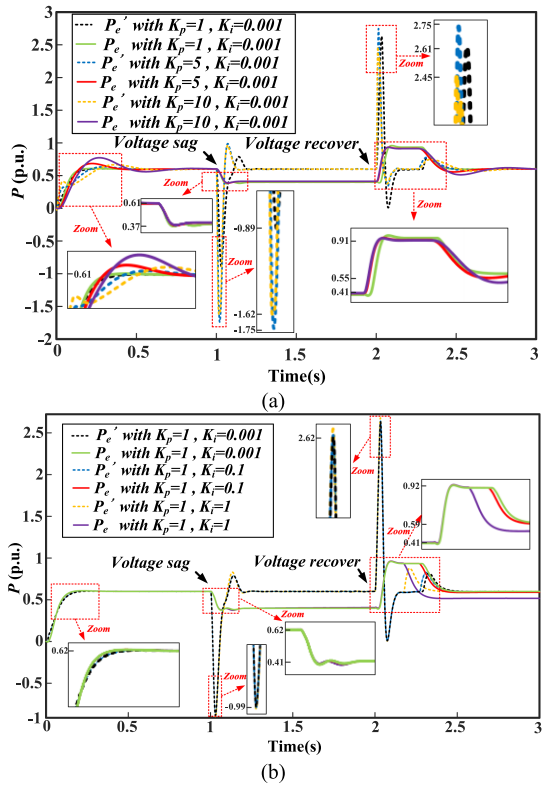

Fig. 10. Time response of P_e and P_e' for different VPC parameters. (a) Proportional coefficient K_p. (b) Integral coefficient K_i.

When the grid voltage level drops from 1.0 to 0.8 p.u., current limiting is not triggered. As a result, the power angle curves shown in Figs. 5(a) and 9(c) are highly similar, indicating similar operational mechanisms. Fig. 9(d) shows the change of $\dot{\delta}-\delta$ during voltage transient drop to 0.8 p.u. and recovery to 1.0 p.u. During a voltage sag, VPA will increase to the equilibrium point b, and VPA will decrease to the equilibrium point a when voltage fault removal, aligning closely with the power angle curve shown in Figs. 5(a) and 9(c).

From the above analysis, it can be found that the introduction of VPC in the active power control loop can keep the power angle stable under large disturbances, and the improved current limiting strategy enhances the recovery capability after fault removal.

D. Influence of VPC Parameters on Active Power

Fig. 10 shows the active power response under different VPC parameters, where the grid voltage drops to 0.5 p.u. at 1–2 s. At this point, $P_{\text{set}} > 1.5 I_{\text{lim}} V_{g\text{SAG}}$ is satisfied and the converter will operate in a current-limited state. According to the analysis of Section III-B, it does not exist a stable power angle when $P_{\text{set}} > 1.5 I_{\text{lim}} V_{g\text{SAG}}$, thus the VSG by itself cannot operate stably. From Fig. 10, it can be found that the actual output power of VSG $P_e < P_{\text{set}}$ in 1–2 s (see solid line). This discrepancy is addressed through introducing VPC, which compensates for the

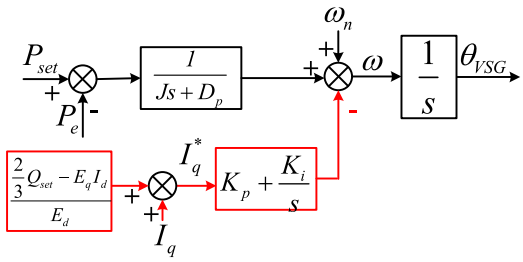

Fig. 11. Block diagram of the modified VPC.

difference between P_{set} and P_e, achieving $P_e' = P_{\text{set}}$ in the control (see dotted line). Consequently, a stable power angle can still be maintained under large disturbances.

Fig. 10(a) shows the time response of P_e and P_e' under different proportional coefficient K_p. It is apparent that the proportional coefficient influences the degree of overshoot in P_e and P_e'. Specifically, a larger proportional coefficient K_p leads to greater overshooting in P_e and P_e', resulting in system oscillation and slower attainment of steady state. The time responses of P_e and P_e' with different integral coefficient K_i are shown in Fig. 10(b). It is evident that the integral coefficient primarily influences the postfault recovery process. A larger integral coefficient contributes to a quicker transition out of voltage inner loop saturation, enabling a prompt return to normal operation. However, a larger integral coefficient will make VPC affect the power angle characteristics after fault recovery. This may result in the actual power output P_e falling below the set value P_{set} after recovery. Thus, the integral coefficient should not be too large to avoid over-saturation of the VPC and interference with the power angle characteristics in the nonfault state.

E. Modified VPC Strategy

The VSG may need to transmit a certain amount of reactive power to meet the demands of the grid. To this end, the proposed VPC strategy requires the following modifications.

Fig. 11 shows the block diagram of the modified VPC implementation, where the feedback input I_q shown in Fig. 6 is changed to I_q^*. According to (2), the definition of I_q^* is given as follows:

$$I_q^* = I_q + \frac{\frac{2}{3}Q_{\text{set}} - E_{\text{q}} I_d}{E_{\text{d}}}. \tag{24}$$

Further simplification can be considered as

$$I_q^* \approx I_q + \frac{2Q_{\text{set}}}{3E_{\text{d}}}. \tag{25}$$

According to (16), and neglecting smaller components, E_d can be approximated as

$$E_d \approx V_{g\text{SAG}} \cos\delta. \tag{26}$$

After introducing the new feedback input I_q^*, (15) can be rewritten as follows:

$$sP_e' = sP_e + s^2 I_q^* J K_p + sI_q^*(JK_i + D_p K_p) + I_q^* D_p K_i. \tag{27}$$

Similarly, (18) can be further rewritten as

$$\begin{aligned}\dot{P}'_e &= D_p K_i I_{\mathrm{q}}^* \\ &- \frac{3}{2} I_{\lim} V_{g\mathrm{SAG}} \dot{\delta} \sin\delta - \frac{(JK_i + D_p K_p)}{I_q} \left(\frac{V_{g\mathrm{SAG}}^2 \sin\delta\cos\delta}{X_\Sigma^2} \right) \dot{\delta} \\ &- \frac{JK_p}{I_q} \left(\frac{V_{g\mathrm{SAG}}^2 \sin\delta\cos\delta}{X_\Sigma^2} \right) \ddot{\delta} + \frac{JK_p}{I_q} \left(\frac{V_{g\mathrm{SAG}} \sin\delta}{X_\Sigma} \right)^2 \dot{\delta}^2 \\ &- \frac{JK_p}{I_q} \left(\frac{V_{g\mathrm{SAG}} \cos\delta}{X_\Sigma} \right)^2 \dot{\delta}^2 - \frac{JK_p}{I_q^3} \left(\frac{V_{g\mathrm{SAG}}^2 \sin\delta\cos\delta}{X_\Sigma^2} \right)^2 \dot{\delta}^2 \\ &+ \frac{2}{3} \frac{Q_{\mathrm{set}}(JK_i + D_p K_p)}{V_{g\mathrm{SAG}}} \sec\delta\tan\delta\,\dot{\delta} + \frac{2}{3} \frac{Q_{\mathrm{set}} JK_p}{V_{g\mathrm{SAG}}} \\ &\times \left(\sec\delta\tan^2\delta\,\dot{\delta} + \sec^3\delta\,\dot{\delta} + \sec\delta\tan\delta\,\ddot{\delta} \right) = 0. \end{aligned} \tag{28}$$

According to (28), it can be inferred that the condition for the steady state of the system is $I_q^* = 0$. That is to say, a certain amount of reactive power Q_{set} can be transmitted.

The above analysis demonstrates that the introduction of VPC achieves power angle stabilization during large disturbances. This effectively compensates for the difference between the output power P_e and the set power P_{set} caused by current limiting. As a result, a stable VPA remains under large disturbances, thereby avoiding transient instability. By reasonably selecting the control parameters within the VPC, it is possible to ensure that the VSG operates smoothly during faults and quickly returns to normal operation once the faults are cleared. If modifications are made to the VPC, it is possible to achieve a certain level of reactive power transmission while also keeping the existing transient stability performance to some extent.

V. Experimental Results

A. Hardware Setup

Due to the complex operations involving grid voltage faults, long-distance transmission, and power converter fault ride-through testing, HIL testing is employed for experimental validation. HIL testing enables model-based interaction with the real environment, ensuring comprehensive validation of the system. Fig. 12 shows the experimental setup. The real-time simulator RT-LAB (OP4050) is used to model power circuits, while the control circuits are implemented by dSPACE. Real-time simulation is conducted through fast data exchange between dSPACE and RT-LAB via their corresponding ports. MicroLabBox (dSPACE company, Germany) samples the RT-LAB output signals (e.g., grid voltage, current, frequency, active and reactive power, etc.) for control law generation. The parameters of the power and control circuits are shown in Table I.

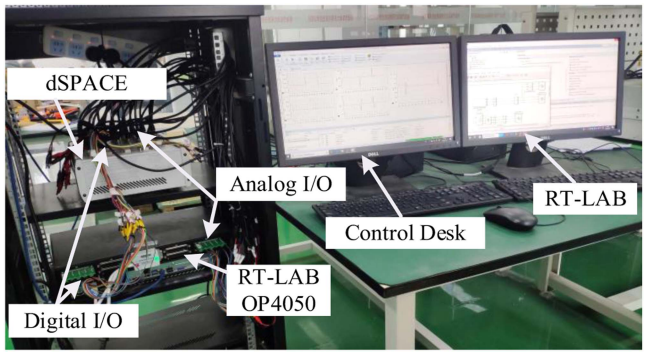

Fig. 12. Configuration of HIL experimental platform.

TABLE I
Parameter Specifications of VSG System in Fig. 1

Parameter	Symbol	Value
DC-link voltage	V_{dc}	800 V
Base value of power	S_n	10 kVA
Normal value of angular frequency	ω_n	100π rad/s
Switching frequency	f_{sw}	5 kHz
Inductor of LC filter	L_1	2 mH
Capacitor of LC filter	C_1	10 μF
Inductance of the line	L_{line}	12 mH
Resistance of the line	R_{line}	0.1 Ω
Rated voltage of grid	V_g	311 V
Rated voltage of PCC	V_0	311 V
Droop coefficient of active power loop	D_p	1591.5 W·s/rad
The inertial coefficient of active power loop	J	15.86 W·s^2/rad
Integral coefficient of reactive power loop	K_q	0.5
Active power reference	P_{set}	0.6 p.u.
Reactive power reference	Q_{set}	0
Allowable current amplitude	I_{lim}	20 A
Sample time	T_s	40 μs
Voltage inner loop PI control parameters	K_{pvc}, K_{ivc}	0.5, 10
Current inner loop PI control parameters	K_{pcc}, K_{icc}	10, 20
PI parameters for VPC	K_p, K_i	1, 0.001

B. Results and Analysis

1) Grid Voltage Drops to 0.5 p.u.: Fig. 13 shows the time response of the VSG with the conventional current limiting-only operation. The output current of the VSG reaches the limiting amplitude after the grid voltage is temporarily dropped from 1.0 to 0.5 p.u. At this time, the system operates in the current saturation mode, leading to oscillations and instability. This is due to the power output capability of the VSG does not meet the requirements of the power reference value, thereby resulting in the absence of a stable VPA. Fig. 13(a) and (b) shows that during the voltage sag, the voltage amplitude, and active and reactive power output from the VSG continue to oscillate. Additionally, the VSG absorbs energy from the grid, exacerbating the instability of the system. After the voltage is restored to 1.0 p.u., conventional VSG is unable to exit the saturated state, preventing it from returning to its initial operating state. Consequently, the system operates at point d as depicted in Fig. 4(b) of Section III, which is abnormal and is to be avoided. The conventional VSG cannot be stabilized when the voltage drops to 0.5 p.u., i.e., it cannot be operated under the condition

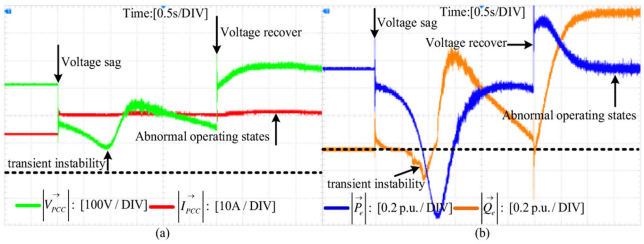

Fig. 13. Response of VSG with conventional control when grid voltage drops to 0.5 p.u. (a) Responses of voltage and current. (b) Responses of active and reactive power.

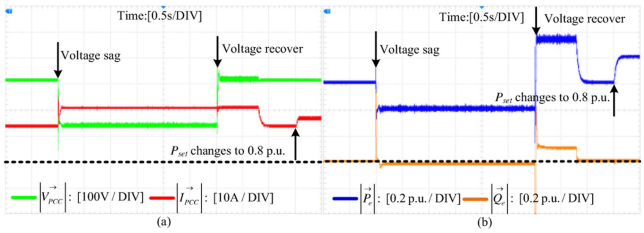

Fig. 14. Response of VSG with VPC when grid voltage drops to 0.5 p.u. (a) Responses of voltage and current. (b) Responses of active and reactive power.

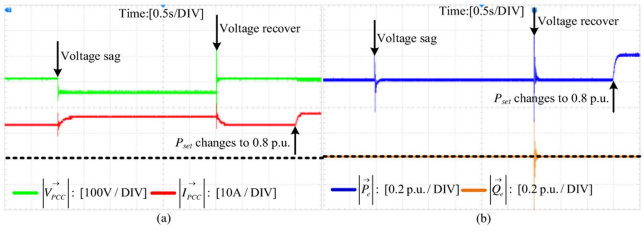

Fig. 15. Response of VSG with conventional control when grid voltage drops to 0.8 p.u. (a) Responses of voltage and current. (b) Responses of active and reactive power.

of satisfying $P_{\text{set}} > 1.5 I_{\text{lim}} V_{g\text{SAG}}$, and it cannot be restored to its original state after the voltage returns to 1.0 p.u.

Fig. 14 shows the time response of the VSG with the VPC. VPC compensates for the power output capability during low-voltage faults through control adjustment, thereby preventing the VSG from instability. Fig. 14(a) and (b) shows that the output voltage, active and reactive power of the VSG can be kept constant without oscillations during the voltage transient drop to 0.5 p.u. The active power is basically maintained at 0.4 p.u., the reactive power is basically maintained at 0 p.u., and the output current is kept running at the maximum limit value. After the voltage returns to 1.0 p.u., the VSG takes about 0.5 s to desaturate and then automatically returns to its original state. The recovered VSG can then respond appropriately to power regulation demands, demonstrating that the VSG retains the capability to mimic the operation of synchronous generators as it did before the fault occurred. It is further demonstrated that the introduction of VPC does not change the steady-state operation point during the nonfault period.

2) Grid Voltage Drops to 0.8 p.u.: From Figs. 15 and 16, one can see that they are very similar. After the voltage is temporarily

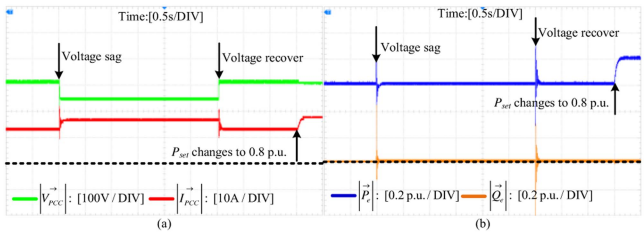

Fig. 16. Response of VSG with VPC when grid voltage drops to 0.8 p.u. (a) Responses of voltage and current. (b) Responses of active and reactive power.

reduced to 0.8 p.u., given that the power output capacity of the VSG at this point can satisfy the power reference value requirements, the system maintains a stable VPA. The current will not reach its limit value, preventing destabilization. Therefore, there is no necessity to introduce an additional VPC as the VSG alone can operate effectively. The currents in Figs. 15(a) and 16(a) are below 20 A, with the output voltage and current amplitude of the VSG remaining constant throughout the fault duration. The active power in Figs. 15(b) and 16(b) remain constant at the power reference value of 0.6 p.u. and the reactive power remains around 0, indicating that the system can track the given value. After fault recovery, both the traditional VSG and the VSG with VPC can restore normal operation, demonstrating that the VSG is capable of meeting the power regulation requirements. The introduction of VPC does not have a negative impact. As a result, the conventional VSG and the VSG with VPC exhibit similar dynamic and static behaviors when $P_{\text{set}} < 1.5 I_{\text{lim}} V_{g\text{SAG}}$ is satisfied, aligning perfectly with the prior analysis.

C. Summary

The above experimental results show that conventional VSG exhibits transient instability during voltage drops to 0.5 p.u. ($P_{\text{set}} > 1.5 I_{\text{lim}} V_{g\text{SAG}}$). Additionally, in this scenario, VSG is unable to recover to normal operation when the fault is cleared. However, the proposed VSG with VPC can work well during voltage sag and has fault recovery capability. It is also demonstrated that the VPC neither changes the steady-state operating point in a normal state nor does it have a negative impact under $P_{\text{set}} < 1.5 I_{\text{lim}} V_{g\text{SAG}}$ is satisfied.

VI. Conclusion

In this article, the transient characteristics of the VSG under two operating conditions are analyzed using power angle curves and the nonlinear features such as current limiting are considered. It is observed that transient instability occurs when the VPA of the VSG surpasses the critical clearing angle under grid voltage sag. The reason for transient instability is that the power transfer capability of the system cannot meet the requirements of the power reference after fault, which leads to the loss of synchronization between the control coordinate and the grid reference coordinate. Based on this, a VPC strategy combined with an improved current limiting strategy has been introduced to enhance the transient stability and fault recovery capability. This strategy aims to ensure that the system's power transfer

capability can meet the power command requirements in control, thereby establishing a stable VPA to prevent transient instability. The proposed VPC strategy is simple and easy to implement, eliminating the need for fault detection, online control switching, and power reference adjustment. However, we have not yet considered the effectiveness of VPC in some cases (e.g., asymmetric fault, multi-VSG system, reactive power injection that is proportional to voltage sag during faults, and low-voltage microgrids with large line impedance ratios R/X). This will be the future research.

REFERENCES

[1] J. Lei, X. Xiang, B. Liu, W. Li, and X. He, "Transient stability analysis of grid forming converters based on damping energy visualization and geometry approximation," *IEEE Trans. Ind. Electron.*, vol. 71, no. 3, pp. 2510–2521, Mar. 2024.

[2] J. Lei, Z. Qin, W. Li, P. Bauer, and X. He, "Stability region exploring of shunt active power filters based on output admittance modeling," *IEEE Trans. Ind. Electron.*, vol. 68, no. 12, pp. 11696–11706, Dec. 2021.

[3] Z. Shuai, Y. Hu, Y. Peng, C. Tu, and Z. J. Shen, "Dynamic stability analysis of synchronverter-dominated microgrid based on bifurcation theory," *IEEE Trans. Ind. Electron.*, vol. 64, no. 9, pp. 7467–7477, Sep. 2017.

[4] M. Chen, D. Zhou, and F. Blaabjerg, "Enhanced transient angle stability control of grid-forming converter based on virtual synchronous generator," *IEEE Trans. Ind. Electron.*, vol. 69, no. 9, pp. 9133–9144, Sep. 2022.

[5] X. Meng, J. Liu, and Z. Liu, "A generalized droop control for grid-supporting inverter based on comparison between traditional droop control and virtual synchronous generator control," *IEEE Trans. Power Electron.*, vol. 34, no. 6, pp. 5416–5438, Jun. 2019.

[6] X. Xiong, C. Wu, and F. Blaabjerg, "Effects of virtual resistance on transient stability of virtual synchronous generators under grid voltage sag," *IEEE Trans. Ind. Electron.*, vol. 69, no. 5, pp. 4754–4764, May 2022.

[7] W. Si and J. Fang, "Transient stability improvement of grid-forming converters through voltage amplitude regulation and reactive power injection," *IEEE Trans. Power Electron.*, vol. 38, no. 10, pp. 12116–12125, Oct. 2023.

[8] H. Cheng, Z. Shuai, C. Shen, X. Liu, Z. Li, and Z. J. Shen, "Transient angle stability of paralleled synchronous and virtual synchronous generators in islanded microgrids," *IEEE Trans. Power Electron.*, vol. 35, no. 8, pp. 8751–8765, Aug. 2020.

[9] C. Luo, X. Ma, T. Liu, and X. Wang, "Controller-saturation-based transient stability enhancement for grid-forming inverters," *IEEE Trans. Power Electron.*, vol. 38, no. 2, pp. 2646–2657, Feb. 2023.

[10] H. Wu and X. Wang, "Design-oriented transient stability analysis of grid-connected converters with power synchronization control," *IEEE Trans. Ind. Electron.*, vol. 66, no. 8, pp. 6473–6482, Aug. 2019.

[11] L. Huang, H. Xin, Z. Wang, L. Zhang, K. Wu, and J. Hu, "Transient stability analysis and control design of droop-controlled voltage source converters considering current limitation," *IEEE Trans. Smart Grid.*, vol. 10, no. 1, pp. 578–591, Jan. 2019.

[12] M. G. Taul, X. Wang, P. Davari, and F. Blaabjerg, "Current limiting control with enhanced dynamics of grid-forming converters during fault conditions," *IEEE J. Emerg. Sel. Topics Power Electron.*, vol. 8, no. 2, pp. 1062–1073, Jun. 2020.

[13] Z. Shuai, C. Shen, X. Liu, Z. Li, and Z. J. Shen, "Transient angle stability of virtual synchronous generators using Lyapunov's direct method," *IEEE Trans. Smart Grid.*, vol. 10, no. 4, pp. 4648–4661, Jul. 2019.

[14] B. Fan and X. Wang, "Equivalent circuit model of grid-forming converters with circular current limiter for transient stability analysis," *IEEE Trans. Power Syst.*, vol. 37, no. 4, pp. 3141–3144, Jul. 2022.

[15] K. G. Saffar, S. Driss, and F. B. Ajaei, "Impacts of current limiting on the transient stability of the virtual synchronous generator," *IEEE Trans. Power Electron.*, vol. 38, no. 2, pp. 1509–1521, Feb. 2023.

[16] S. P. Me et al., "Transient stability analysis of virtual synchronous generator equipped with quadrature-prioritized current limiter," *IEEE Trans. Power Electron.*, vol. 38, no. 9, pp. 10547–10553, Sep. 2023.

[17] P. Rodriguez, A. V. Timbus, R. Teodorescu, M. Liserre, and F. Blaabjerg, "Flexible active power control of distributed power generation systems during grid faults," *IEEE Trans. Ind. Electron.*, vol. 54, no. 5, pp. 2583–2592, Oct. 2007.

[18] K. Shi, W. Song, P. Xu, R. Liu, Z. Fang, and Y. Ji, "Low-voltage ride-through control strategy for a virtual synchronous generator based on smooth switching," *IEEE Access*, vol. 6, pp. 2703–2711, 2018.

[19] K. O. Oureilidis and C. S. Demoulias, "A fault clearing method in converter-dominated microgrids with conventional protection means," *IEEE Trans. Power Electron.*, vol. 31, no. 6, pp. 4628–4640, Jun. 2016.

[20] H. Wu and X. Wang, "A mode-adaptive power-angle control method for transient stability enhancement of virtual synchronous generators," *IEEE J. Emerg. Sel. Topics Power Electron.*, vol. 8, no. 2, pp. 1034–1049, Jun. 2020.

[21] X. Lu, J. Wang, J. M. Guerrero, and D. Zhao, "Virtual-impedance-based fault current limiters for inverter dominated ac microgrids," *IEEE Trans. Smart Grid.*, vol. 9, no. 3, pp. 1599–1612, May 2018.

[22] A. D. Paquette and D. M. Divan, "Virtual impedance current limiting for inverters in microgrids with synchronous generators," *IEEE Trans. Ind Appl.*, vol. 51, no. 2, pp. 1630–1638, Mar./Apr. 2015.

[23] S. F. Zarei, H. Mokhtari, M. A. Ghasemi, and F. Blaabjerg, "Reinforcing fault ride through capability of grid forming voltage source converters using an enhanced voltage control scheme," *IEEE Trans. Power Del.*, vol. 34, no. 5, pp. 1827–1842, Oct. 2019.

[24] A. Camacho, M. Castilla, J. Miret, A. Borrell, and L. G. de Vicuña, "Active and reactive power strategies with peak current limitation for distributed generation inverters during unbalanced grid faults," *IEEE Trans. Ind. Electron.*, vol. 62, no. 3, pp. 1515–1525, Mar. 2015.

[25] T. Wen, "Power coupling mechanism analysis and improved decoupling control for virtual synchronous generator," *IEEE Trans. Power Electron.*, vol. 36, no. 3, pp. 3028–3041, Mar. 2021.

[26] B. Fan and X. Wang, "Fault recovery analysis of grid-forming inverters with priority-based current limiters," *IEEE Trans. Power Syst.*, vol. 38, no. 6, pp. 5102–5112, Nov. 2023.

Bo Long (Senior Member, IEEE) received the B.S. degree in electrical engineering from Xi'an Petroleum University, Xi'an, China, in 2001, and the Ph.D. degree in electrical engineering from Xi'an Jiaotong University, Xi'an, China, in 2008.

In 2008, he joined the Department of Power Electronics, School of Mechatronics Engineering, University of Electronic Science and Technology of China (UESTC), Huzhou, P.R. China, where he has been an Associate Professor since 2014. He is currently the supervisor for eleven master's students, two of which have been nominated as provincial outstanding graduate students of UESTC. His research interests include grid-connected converters for renewable energy systems and distributed generation system (DGs), model predictive control, power quality, multilevel converters, ac motor control, and resonance suppression techniques for smart grid applications.

Dr. Long is an active Reviewer for IEEE TRANSACTIONS ON POWER ELECTRONICS, *ISA Transactions*, *Applied Energy*, *Energy*, IEEE TRANSACTIONS ON SMART GRID, IEEE TRANSACTIONS ON INDUSTRIAL ELECTRONICS, IEEE TRANSACTIONS ON SUSTAINABLE ENERGY, and IEEE TRANSACTIONS ON ENERGY CONVERSION.

ChengKun Hu received the B.S. degree in electrical engineering and automation from Shanghai Maritime University, Shanghai, China, in 2022. He is currently working toward the M.S. degree in electrical engineering with the University of Electronic Science and Technology of China, Chengdu, China.

His research interests include fractional order modeling and control, model predictive control, virtual synchronous generator control, and parametric robustness of power electronic systems.

ZhiHao Chen received the B.S. degree in electrical engineering and automation from Northwest A&F University, Xianyang, China, in 2022. He is currently working toward the M.S. degree in electrical engineering with the University of Electronic Science and Technology of China, Chengdu, China.

His research interests include leakage current reduction methods for grid-connected inverters and model predictive control methods for common mode voltage reduction.

Jiefeng Hu (Senior Member, IEEE) received the Ph.D. degree in electrical engineering from the University of Technology Sydney, Ultimo, NSW, Australia, in 2013.

He participated in the research of minigrids at the Commonwealth Scientific and Industrial Research Organization, Newcastle, NSW, Australia. He was an Assistant Professor with The Hong Kong Polytechnic University, Hong Kong. He is currently an Associate Professor and a Program Coordinator of Electrical Engineering with the Federation University Australia, Ballarat, VIC, Australia, where he is also the Stream Leader with the Centre for New Energy Transition Research. He is currently with the Centre for New Energy Transition Research, Federation University Australia, Mount Helen, VIC, Australia, and the Australia Institute of Innovation, Science and Sustainability, Federation University Australia, Mount Helen, VIC, Australia. His research interests include power electronics, renewable energy, and smart microgrids.

Dr. Hu is currently an Associate Editor for *IET Renewable Power Generation*, an Editor IEEE TRANSACTIONS ON ENERGY CONVERSION, and an Associate Editor for IEEE ACCESS. He was a Guest Editor for IEEE TRANSACTIONS ON INDUSTRIAL ELECTRONICS for a Special Issue "Applications of Predictive Control in Microgrids."

José Rodríguez (Life Fellow, IEEE) received the Engineering degree in electrical engineering from the Universidad Tecnica Federico Santa Maria, Valparaiso, Chile, in 1977, and the Dr.-Ing. degree in electrical engineering from the University of Erlangen, Erlangen, Germany, in 1985.

Since 1977, he has been with the Department of Electronics Engineering, Universidad Tecnica Federico Santa Maria, where he was a Full Professor and the President. From 2015 to 2019, he was the President of Universidad Andres Bello, Santiago, Chile. Since 2022, he has been the President of Universidad San Sebastian, Santiago. He has coauthored two books, several book chapters, and more than 700 journal and conference papers. His research interests include multilevel inverters, new converter topologies, control of power converters, and adjustable-speed drives.

Dr. Rodriguez was the recipient of several best paper awards from journals of IEEE, the National Award of Applied Sciences and Technology from the Government of Chile in 2014, and the Eugene Mittelmann Award from the Industrial Electronics Society of the IEEE in 2015. He is Member of the Chilean Academy of Engineering. In 2014.2020, he was included in the list of Highly Cited Researchers published by Web of Science.